Journal Pre-proof

Energy-efficient Electronics with an Air-friction-driven Rotating Gate Transistor using Tribotronics

Hyunji Shin, Dae Yu Kim

Please cite this article as: Shin, H., Kim, D.Y., Energy-efficient Electronics with an Air-friction-driven Rotating Gate Transistor using Tribotronics, *ISCIENCE* (2024), doi: https://doi.org/10.1016/j.isci.2024.109029.

This is a PDF file of an article that has undergone enhancements after acceptance, such as the addition of a cover page and metadata, and formatting for readability, but it is not yet the definitive version of record. This version will undergo additional copyediting, typesetting and review before it is published in its final form, but we are providing this version to give early visibility of the article. Please note that, during the production process, errors may be discovered which could affect the content, and all legal disclaimers that apply to the journal pertain.
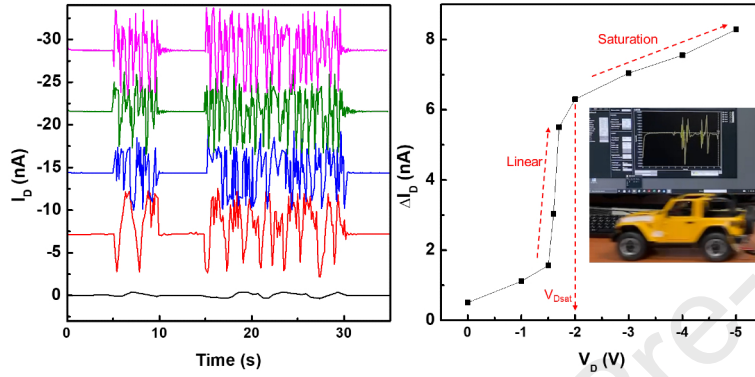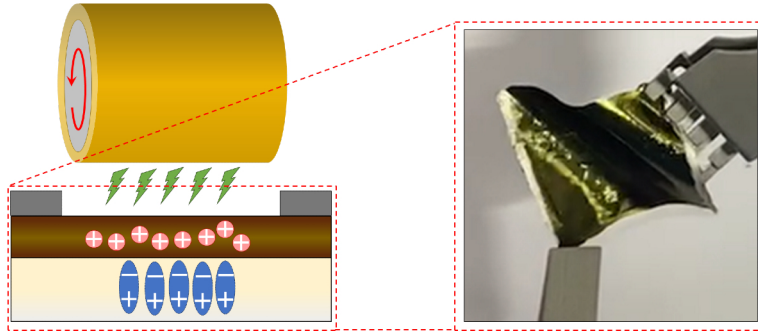
Energy-efficient Electronics with an Air-friction-driven Rotating Gate Transistor using Tribotronics

Hyunji Shin [1, 2, 3]**, Dae Yu Kim** [2, 3, 4, *]

SUMMARY

Concern for the environment is one of the main factors that are increasing the demand for compact and energy-efficient electronic devices. Recent research has made advances in reducing the power consumption of field-effect transistors, including the use of high-dielectric insulators, low-voltage operation, and selective power-conservation strategies. This paper introduces a revolutionary air-friction-driven rotating gate transistor that operates without the need for a conventional gate voltage. This new device offers the advantages of wear resistance, a slim and flexible design (achieved through low-temperature solution processing), and a simplified three-layer structure that streamlines manufacturing and reduces potential carbon emissions. This device's wear resistance and ease of fabrication render the device a promising technology with applications in various fields, including electronics, vehicles, aviation, and wearable devices. This study provides evidence of the device's feasibility for use in real-world vehicular scenarios, underscoring its potential for future innovation and widespread adoption.

[1] School of Semiconductor Display Technology, Hallym University, Chuncheon 24252, Republic of Korea

[2] Department of Electrical and Computer Engineering, Inha University, Incheon 22212, Republic of Korea

[3] Center for Sensor Systems, Inha University, Incheon 22212, Republic of Korea

[4] Lead contact

[*] Correspondence: dyukim@inha.ac.kr

INTRODUCTION

Field effect transistors (FETs) have been employed extensively in the field of flexible electronic devices, which encompasses biosensors and chemical sensors,[1,2] displays,[3] and memory modules.[4,5] These technological advancements have significantly increased the deployment of FETs various fields while simultaneously expediting the evolution of intelligent systems and wearable technologies. Moreover, the electronics domain is demanding increasing integration into compact form factors, with a concurrent emphasis on power efficiency, which has increased in recent years.[6–8] From an environmental perspective, the drive to reduce greenhouse gas emissions and transition toward sustainable energy is increasing within the electronics field. Industry-wide, a concerted focus exists on reducing carbon footprints, with research and development efforts actively contributing toward this goal.[9–12] Recent contributions to the achievement of this goal have included the introduction of an insulator with a high dielectric constant and a FET that operates at voltages as low as 2 V, which was reported by Tetzner et al.[13] Furthermore, the fundamental power consumption of FETs has been minimized, with a subthreshold slope as low as 65 mV/decade owing to the use of high-purity rubrene single crystals, as demonstrated by Blülle et al.[14] Moreover, Jo et al.[15] introduced a selective scan driver and presented a circuit configuration aimed at conserving power that would otherwise be wasted. In addition to these studies, research with a distinct emphasis on low-power-consumption FETs has recently increased.[16–19]

Phototransistors offer an alternate route to achieving energy efficiency by harnessing sustainable light energy.[20–24] However, similar to solar cells, the efficiencies of most phototransistors decrease with increasing temperature, resulting in increased leakage current and decreased energy yield. Ongoing research is attempting to mitigate these thermal losses without using extensive cooling systems or heat-load management.[25–28] Furthermore, this research direction has resulted in an innovative paradigm shift in which the traditional gate voltage (V_G) in FETs has been supplanted by voltage sourced directly from triboelectric nanogenerators (TENGs) to significantly reduce power consumption.[29–38] These systems are attractive due to their eco-friendly promise of harnessing electrical energy from wasted ambient mechanical energy.[39] However, the FET's reliance on TENGs for supplying the V_G necessitates an additional component, which complicates the fabrication process and deviates from the trend of miniaturization. The rotating gate transistor presented by Shin et al.[40] addressed this challenge by capitalizing on the triboelectric effect caused by friction between the gate and the insulating layer, yielding a compact low-power FET through structural

streamlining. However, persistent high-speed friction during device operation can cause rapid wear, compromising the device's longevity.

In response to the aforementioned issues, we introduce the air friction-driven rotating gate transistor (AFRGT), which is a groundbreaking concept in which the transistor is operated exclusively by the application of a drain voltage (V_D) and proximity to a rotating component, without the requirement of an applied V_G. The AFRGT features a rotating gate that operates in a non-contact mode (to ensure wear resistance) combined with a slim, flexible form factor facilitated by low-temperature solution processing using organic semiconducting polymers. Notably, the harnessed energy is directly employable for powering purposes; however, the transistor itself possesses a streamlined design that only comprises three layers without any additional components, thereby reducing carbon emissions by simplifying future manufacturing processes. Crucially, the AFRGT dispenses with the conventional notion of a gate and operates by replacing V_G with harvested energy sources from the rotating tires of vehicles. This innovation is a breakthrough because it recycles energy expended during vehicle propulsion.

RESULTS AND DISCUSSION

Channel Formation Mechanism and Device Operation

The process underlying the amplification of the drain current (I_D) within the proposed AFRGT is illustrated in Figure 2. The cross-sectional schematic of the device structure in Figure 2(a) provides a detailed description of the device. Notably, our investigation uncovered a multiple events, the first of which involved the appearance of a negatively charged surface on the rotating gate. As demonstrated in Figure 2(b), this intriguing phenomenon emerged due to the generation of triboelectric charges via the contact electrification between the surrounding polyimide (PI) covering and the aluminum wheel.[41] Notably, the spatial orientation of the rotating gate, including an intentional air gap, isolates the gate from the active layer of the device, as displayed in Figure 2(c). When the gate started rotating, a series of interactions occurred within the vicinity of the device. The gate was in frictional contact with microscopic airborne particles and induced negative charges on them, as depicted in Figures 2(d) and (e). The resulting phenomenon caused by this interaction is displayed in Figure 2(f) in which the negatively charged particles located within the air gap induce hole carriers within the adjacent active layer. This process gained momentum as the rotational speed of the wheel increased, ultimately forming a channel rich in hole carriers. Furthermore, as described in Figure 2(g), the

polarization of the substrate located beneath the active layer increases the electric field, emphasizing the overall dynamics of the process.

On applying a potential difference (V_D between the generated channels), I_D is amplified owing to the utilization of hole carriers, as shown in Figure 3(a). In the previously introduced rotating gate transistor, the gate was in direct frictional contact with the insulator, inducing charges within the adjacent active layer located on the opposite side. Drawing a parallel with this phenomenon, the AFRGT formed channels using the inductive influence of charges within the active layer owing to the friction with the air-gap insulator (i.e., non-frictional interaction). However, the fabricated AFRGT deviated (to an extent) from the standard behavior of conventional FETs. In conventional FETs, channels are formed via dielectric polarization by applying a voltage to the gate. In contrast, channel formation in the AFRGT is a consequence of the air friction exerted on the gate. Regardless of this distinction, the fabricated AFRGT manifested attributes similar to conventional FETs. For example, I_D amplification in the channel owing to the accumulation of charge carriers was discernible within the AFRGT. As demonstrated in Figure 3b, by applying a negative voltage to the drain electrode following the accumulation of holes within the poly(3-hexylthiophene-2,5-diyl) (P3HT) (which is a p-type semiconducting polymer) active layer, the Fermi level (E_F) of the drain electrode increased, promoting an undisturbed flow of holes from the source electrode to the drain electrode.[40,42] This effect contributed to the overall efficacy of the AFRGT's amplification mechanism, enhancing the prospect of practical application.

Figure 4 presents the I_D in response to a gradually decreasing V_D from 0 to −20 V through −5 V being applied between the source and drain (S/D) electrodes. This investigation was conducted with the gate of the fabricated AFRGT in both rotational (driven) and stationary (non-driven) states. The time-dependent graph illustrates the obtained results. These measurements were recorded under the influence of two distinct gating conditions: a bare aluminum gate and a gate coated with PI. When the gate was non-driven, the I_D value corresponding to the applied V_D was consistent. However, I_D was distinctly amplified when the gate was driven. The AFRGT structure is inspired by the FET structure; however, unlike the ideal FET in which I_D is independent of V_D when the applied V_G is zero, the AFRGT operates as a metal-semiconductor-metal structure (which is a source-active layer-drain structure) without V_G. More specifically, prior to the onset of air friction, the I_D of the AFRGT depends on V_D. However, as illustrated in Figure 4, during gate rotation represented by the shaded region, the I_D of the AFRGT is amplified with respect to that under the gate-stopped condition, thereby resembling the application of V_G in a FET. Notably, these fluctuations were pronounced when the gate was coated with a PI layer, unlike when an uncoated aluminum gate was used. Notably, the bare aluminum gate

was not in contact with PI, indicating that it did not generate contact electrification by itself. Furthermore, static electricity is considerably weaker in metallic materials than in polymeric insulating materials.[43] Accordingly, PI exhibits a greater susceptibility to surface charge induction than aluminum, causing a substantial variation in I_D. Moreover, both variants of the device exhibited minimal variations in current at a V_D of 0 V.

Substrate Influence on Current Amplification

To determine the physical significance of these current variations, we explored the impact of poly(vinylidene fluoride) (PVDF) substrate thickness on the device's operation. Figure 4 displays that all the measured I_D values are negative owing to the application of a negative V_D, considering the P-type active layer. However, as displayed in Figure 5, the variations in I_D (ΔI_D) are represented as positive because only the current amplified by the rotation of the gate is extracted and portrayed. Notably, the I_D of each device was averaged across multiple device fabrication and measurement iterations, minimizing any potential experimental discrepancies. In addition to the 50-µm-thick PVDF substrate used in Figure 4, we incorporate PVDF substrates of varying thicknesses (10, 100, 150, and 200 µm). In contrast to the uncoated aluminum gate in Figure 4, all five device variants exhibited high ΔI_D values when subjected to the rotation of the PI-covered gate. Moreover, the overall ΔI_D reached saturation at −5 V with minimal incremental enhancement at V_D values of −10, −15, and −20 V. Notably, excluding the thinnest substrate, which is 10 µm, the devices with 50-, 100-, 150-, and 200-µm-thick PVDF substrates exhibited increasing ΔI_D as the substrate thickness decreased. In particular, the device with a 50 µm PVDF substrate demonstrated the stands out ΔI_D of 9.675 nA under a V_D of −20 V. When other parameters remained constant and only the insulating layer thickness increased, the I_D could be reduced. The following formula delineates the relationship between I_D and insulator thickness (t_{ox}) of a conventional FET:

$$I_{D(Sat)} = \frac{\mu W C_{ox}(V_G - V_T)^2}{2L},$$

$$C_{ox} = \frac{\epsilon_{ox}}{t_{ox}},$$

where $I_{D(Sat)}$ is the I_D in the saturation region, μ is the mobility, C_{ox} is the capacitance, and ϵ_{ox} represents the dielectric constant.[44,45] In the proposed device configuration, the PVDF substrate functions as a secondary insulator after the primary air-gap insulator. This induces electric charges in the active layer via the polarization induced by the electric field, similar to the insulator's role in a traditional FET. Consequently, ΔI_D increased as the PVDF substrate's thickness

decreased apart from a notable reduction in the case of the 10 μm substrate. This phenomenon underscores that the PVDF insulator substrate in the device structure occupies the opposite side of the active layer where air friction occurs, unlike the conventional FET arrangement. Accordingly, the very thin insulator layers often result in charge-to-breakdown in conventional FETs.[46–48] Conversely, insufficient charge induction becomes prominent if the PVDF substrate in the AFRGT is excessively thin.

Saturation Behavior and Dependence of Air-friction Distance

Figure 6(a) illustrates the ΔI_D with respect to V_D across the voltage range of 0 to −5 V, focusing on a device with a 50 μm PVDF substrate. Evidently, ΔI_D exhibited a pronounced surge starting at a V_D of approximately −1.5 V, followed by a marked attenuation as the saturation point of the applied V_D (V_{DSat}) approached −2 V. This trend notably delineated the identifiable transitional regions, similar to the characteristic linear and saturation phases observed in conventional FETs. More specifically, I_D varied due to the channel created by induced and accumulated charges within the active layer.

To further investigate the dependence of air-gap distance on the air-friction-induced charges, a supplementary experiment is conducted, as shown in Figure 6(b). During the experiment, ΔI_D was measured by incrementally adjusting the air gap between 0.5–100 mm while maintaining V_D at −20 V. The results revealed a ΔI_D of 10.57 nA at the minimal proximity of 0.5 mm with a logarithmic decline proportionate to the linear augmentation of distance that culminated in a minute ΔI_D value of 0.08 nA at the maximum separation of 100 mm. Because the active layer was situated in proximity to the air-friction region, the active layer at the minimum distance exhibited a high efficiency in terms of charge induction from charged fine molecules. However, the efficiency of charge induction diminished as the physical distance from the air-friction region increased.

Substrate Variability and Effect of the Absence of an Active Layer on Current Response

Extending our investigation beyond PVDF, we replicated the experiment and employed diverse substrate materials including glass, fluorinated ethylene propylene (FEP), and polydimethylsiloxane (PDMS). Figure 7 presents ΔI_D-versus-V_D graphs obtained from the devices with these alternative substrates. The device fabricated on a glass substrate exhibited the lowest ΔI_D with a progressive escalation in the following sequence: FEP→PDMS→PVDF. This hierarchy was attributed to the dielectric constants and triboelectric polarities of the materials. Glass can be characterized by its dielectric constant of 6.7, and it is the second most polarizable among the four substrates

compared.[49] However, glass was on the positive side of the triboelectric series, rendering it relatively less responsive to charging when in contact with P3HT (the p-type semiconducting polymer active layer).[50,51] In contrast, the dielectric constants of PVDF, PDMS, and FEP are 10.2, 2.77, and 2.1, respectively.[52–55] Aligning with the triboelectric series, the ΔI_D observed across devices incorporating these three substrates all exhibited negative polarity, which closely adhered to the hierarchy dictated by their respective dielectric constants.[56,57]

Figure 8 presents the ΔI_D profiles of the proposed AFRGT device, without a P3HT active layer and subjected to varying V_D values of 0, −10, and −20 V. Across both plots of the bare aluminum and PI-covered gates, a minute current variation of approximately 2 pA was recorded when the gate rotation was stopped. Furthermore, the bare aluminum gate resulted in an ΔI_D of approximately 320 pA during rotation, while the PI-covered gate yielded approximately 440 pA. These ΔI_D values were minute with respect to the ΔI_{DS} observed in previous intact AFRGT devices with active layers and could be attributed to leakage currents traversing the PVDF substrate. This finding substantiated the inference that the observed ΔI_{DS} in all the analyzed AFRGT devices clearly signified that current was amplified through the active P3HT channel layer within the device.

Verification through Practical Application

To evaluate the practical application potential of our fabricated AFRGT in real vehicle scenarios, we conducted an experiment employing the wheels of a radio control (RC) car, as shown in Figure 9. The figure displays the fabrication of the flexible AFRGT device on a PVDF substrate and affixing it to a rigid framework using electrical tape. This assembly provided a reliable platform for connecting the S/D electrodes in Figure 9(b). Subsequently, as presented in Figure 9(c), the framed device was fixed on the mud flap at an approximate distance of 1 mm from the tire of the RC car. A V_D of −20 V was then applied to the wire connected to the S/D electrodes allowing for I_D measurements. The dynamic motion of the RC car's wheel results in a fluctuating I_D profile, whereas the I_D maintains a consistent value when the wheel is stopped, as shown in Figure 9(d). This test confirmed the device's capacity to harness air friction-induced current from the moving tire of the car, proving its applicability in real-world vehicle scenarios.

CONCLUSIONS

In this study, we introduced a novel AFRGT and conducted a comprehensive analysis of its operational principles and characteristics. Our investigation revealed the mechanism responsible for the amplification of I_D in the AFRGT,

different from conventional FETs. Specifically, we identified that the induction of hole carriers in the active layer was the pivotal process resulting in channel formation in the AFRGT. This was achieved through air-friction-driven interactions with the negatively charged surface generated through contact electrification of the rotating gate. Our findings underscore the distinguishing feature of the AFRGT, which eliminates the necessity for a V_G to amplify I_D. Instead, the device relies on the charge induction mechanism owing to air friction. Notably, within the context of a 50-µm-thick PVDF substrate, only −20 V of V_D and proximity of 0.5 mm to the rotating component yielded a substantial variation in I_D (10.57 nA).

Although the presented AFRGT had the advantages of being a non-contact RGT and a gate-free transistor, the output electric current was relatively limited. Realizing the full potential of this innovative transistor technology requires further research and development. In future research, substantial improvements in current output are anticipated through straightforward approaches such as the application of semiconductor materials with high charge mobilities in their active layers instead of P3HT, substitution of insulating substrates with materials exhibiting higher ε_{ox} than PVDF, or increasing the width/length ratio in the active-layer area. By positioning the proposed AFRGT near a rotating object, without any physical contact, the electric current can be amplified. Eliminating the need for a rotating component can simplify the fabrication process, which only comprises three steps in the entire solution process: the substrate, active layer, and S/D electrodes. This streamlined manufacturing process will allow for the fabrication of thin and flexible devices at low temperatures, facilitating a wide array of potential applications. Moreover, the simple structure and low-temperature solution processing of this technology will yield significant environmental benefits by conserving energy resources required for material fabrication and vacuum processes. Additionally, the inherent wear-resistant characteristics through non-friction will confer permanence to the device, resulting in cost savings related to production. Furthermore, the AFRGT aligns with the concept of sustainable development by harvesting and utilizing the energy expended by rotating tires during the straightforward movement of vehicles.

Significantly, our experimental results involving the wheels of an RC car provided substantial evidence of the AFRGT's feasibility. The device adeptly harnessed electric current generated through air friction from moving tires, demonstrating its practicality and applicability in real-world environments. This underscores the promising prospects of AFRGT technology across diverse domains ranging from electronics to vehicle systems with considerable interests and potential for future innovation. Moreover, various applications of this technology extend beyond the integration

of current amplifiers and switches to harness external aerodynamic forces during vehicular and aviation operations. The AFRGT can also be employed as a power-assist device by storing amplified currents.

Limitations of the Study

Because the P3HT layer is delicate and thin, experiments involving rotating the gate directly with the P3HT film with a bottom electrode were not conducted. Opting for a resilient and robust active layer may effectively address the inherent output performance of the rotating TENG. This approach allows for the quantification of the equivalent gate voltage. Since our AFRGT is fabricated from polymer materials, temperature variations can influence the material itself, leading to changes in its properties. Furthermore, our measurement equipment faces challenges in measuring below the ~ nA level, and the output current of our device is at the ~nA level. Thus, despite conducting experiments at low speeds to extract data, measuring the anticipated gradual changes proved to be insufficient. We aim to develop an improved AFRGT through future advanced research moving forward, achieving enhanced robustness and output performance. This will enable us to test the device under various speed and temperature conditions.

Author contributions

H.S.: Conceptualization, Methodology, Validation, Formal analysis, Investigation, Resources, Data Curation, Writing - Original Draft, Writing - Review & Editing, Visualization, Supervision, Project administration. D.Y.K.: Conceptualization, Resources, Writing - Review & Editing, Supervision, Funding acquisition,

Declaration of interests

The authors declare no competing interests.

REFERENCES

1.   Luo, L., and Liu, Z. (2022). Recent progress in organic field-effect transistor-based chem/bio-sensors. View *3*, 20200115. 10.1002/VIW.20200115.

2.   Fan, Y., Liu, J., Hu, W., Liu, Y., and Jiang, L. (2020). The effect of thickness on the optoelectronic properties of organic field-effect transistors: towards molecular crystals at monolayer limit. J Mater Chem C Mater *8*, 13154–13168. 10.1039/D0TC03193C.

3.   Lee, H., Kim, D., Shin, H., Bae, J.H., and Park, J. (2023). Effects of Post-UV/Ozone Treatment on Electrical Characteristics of Solution-Processed Copper Oxide Thin-Film Transistors. Nanomaterials 2023, Vol. 13, Page 854 *13*, 854. 10.3390/NANO13050854.

4.   Han, S., Kim, Y., Son, D., Baac, H.W., Won, S.M., and Shin, C. (2022). Study on memory characteristics of fin-shaped feedback field effect transistor. Semicond Sci Technol *37*, 065006. 10.1088/1361-6641/AC643E.

5.   Kim, J., Ho, D., Kim, I.S., Kim, M.G., Baeg, K.J., and Kim, C. (2021). Solution-processed flexible nonvolatile organic field-effect transistor memory using polymer electret. Org Electron *99*, 106331. 10.1016/J.ORGEL.2021.106331.

6.   Duan, Y., Zhang, B., Zou, S., Fang, C., Wang, Q., Shi, Y., and Li, Y. (2020). Low-power-consumption organic field-effect transistors. Journal of Physics: Materials *3*, 014009. 10.1088/2515-7639/AB6305.

7.   Sirringhaus, H. (2009). Reliability of Organic Field-Effect Transistors. Advanced Materials *21*, 3859–3873. 10.1002/ADMA.200901136.

8.   Sirringhaus, H. (2014). 25th Anniversary Article: Organic Field-Effect Transistors: The Path Beyond Amorphous Silicon. Advanced Materials *26*, 1319–1335. 10.1002/ADMA.201304346.

9.   Xu, G., Li, X., Fu, J., Zhou, Y., Xia, X., and Zi, Y. (2023). Environmental lifecycle assessment of CO2-filled triboelectric nanogenerators to help achieve carbon neutrality. Energy Environ Sci *16*, 2112–2119. 10.1039/D2EE04119G.

10.   Cai, L., Luo, J., Wang, M., Guo, J., Duan, J., Li, J., Li, S., Liu, L., and Ren, D. (2023). Pathways for municipalities to achieve carbon emission peak and carbon neutrality: A study based on the LEAP model. Energy *262*, 125435. 10.1016/J.ENERGY.2022.125435.

11. Wang, Y.M., Zeng, Q., He, L., Yin, P., Sun, Y., Hu, W., and Yang, R. (2021). Fabrication and application of biocompatible nanogenerators. iScience *24*, 102274. 10.1016/J.ISCI.2021.102274.

12. Ouyang, B., Zhang, K., and Yang, Y. (2018). Photocurrent Polarity Controlled by Light Wavelength in Self-Powered ZnO Nanowires/SnS Photodetector System. iScience *1*, 16–23. 10.1016/j.isci.2018.01.002.

13. Tetzner, K., Schroder, K.A., and Bock, K. (2014). Photonic curing of sol–gel derived HfO2 dielectrics for organic field-effect transistors. Ceram Int *40*, 15753–15761. 10.1016/J.CERAMINT.2014.07.099.

14. Blülle, B., Häusermann, R., and Batlogg, B. (2014). Approaching the trap-free limit in organic single-crystal field-effect transistors. Phys Rev Appl *1*, 034006. 10.1103/PHYSREVAPPLIED.1.034006/FIGURES/6/MEDIUM.

15. Jo, J.H., Jeong, W.B., Joung, Y.S., and Lee, S.W. (2022). Selective Scan Driver for Low-Power Consumption Using Oxide Thin Film Transistors. IEEE Electron Device Letters *43*, 1263–1266. 10.1109/LED.2022.3184337.

16. Kumar, P., Gupta, M., Singh, K., and Kumar, N. (2023). Analysis of transition metal dichalcogenides materials based gas sensor using non-equilibrium green's function. International Journal of Numerical Modelling: Electronic Networks, Devices and Fields *36*. 10.1002/jnm.3036.

17. Ranjan, R., Raman, A., Kumar, P., and Kumar, N. (2023). Design and investigation of extended source F-type nano field effect transistor using non-equilibrium Green's function. Micro and Nanostructures *182*, 207645. 10.1016/j.micrna.2023.207645.

18. Bhardwaj, A., Kumar, P., Raj, B., Kumar, N., and Anand, S. (2023). Design and optimization of vertical nanowire tunnel FET with electrostatic doping. Engineering Research Express *5*, 045025. 10.1088/2631-8695/acff3a.

19. Anam, A., Amin, S.I., Prasad, D., Kumar, N., and Anand, S. (2023). Charge-plasma-based inverted T-shaped source-metal dual-line tunneling FET with improved performance at 0.5 V operation. Phys Scr *98*, 095918. 10.1088/1402-4896/aceb95.

20. Simone, G., Dyson, M.J., Meskers, S.C.J., Janssen, R.A.J., and Gelinck, G.H. (2020). Organic Photodetectors and their Application in Large Area and Flexible Image Sensors: The Role of Dark Current. Adv Funct Mater *30*, 1904205. 10.1002/ADFM.201904205.

21. Tavasli, A., Gurunlu, B., Gunturkun, D., Isci, R., and Faraji, S. (2022). A Review on Solution-Processed Organic Phototransistors and Their Recent Developments. Electronics 2022, Vol. 11, Page 316 *11*, 316. 10.3390/ELECTRONICS11030316.

22. Shin, H., Kim, D., Park, J., and Kim, D.Y. (2023). Improving Photosensitivity and Transparency in Organic Phototransistor with Blending Insulating Polymers. Micromachines 2023, Vol. 14, Page 620 *14*, 620. 10.3390/MI14030620.

23. Huang, J., Du, J., Cevher, Z., Ren, Y., Wu, X., and Chu, Y. (2017). Printable and Flexible Phototransistors Based on Blend of Organic Semiconductor and Biopolymer. Adv Funct Mater *27*, 1604163. 10.1002/ADFM.201604163.

24. Shin, H., Lee, H., Kim, B., Zhang, X., Bae, J.-H., and Park, J. (2022). Effects of Blended Poly(3-hexylthiophene) and 6,13-bis(triisopropylsilylethynyl) pentacene Organic Semiconductors on the Photoresponse Characteristics of Thin-Film Transistors. Korean J. Met. Mater.) *60*, 198–205. 10.3365/KJMM.2022.60.3.198.

25. Vaillon, R., Dupré, O., Cal, R.B., and Calaf, M. (2018). Pathways for mitigating thermal losses in solar photovoltaics. Scientific Reports 2018 8:1 *8*, 1–9. 10.1038/s41598-018-31257-0.

26. Wu, Z., Li, N., Eedugurala, N., Azoulay, J.D., Leem, D.S., and Ng, T.N. (2020). Noise and detectivity limits in organic shortwave infrared photodiodes with low disorder. npj Flexible Electronics 2020 4:1 *4*, 1–8. 10.1038/s41528-020-0069-x.

27. Jansen-van Vuuren, R.D., Armin, A., Pandey, A.K., Burn, P.L., and Meredith, P. (2016). Organic Photodiodes: The Future of Full Color Detection and Image Sensing. Advanced Materials *28*, 4766–4802. 10.1002/ADMA.201505405.

28. Aghaei, M., Fairbrother, A., Gok, A., Ahmad, S., Kazim, S., Lobato, K., Oreski, G., Reinders, A., Schmitz, J., Theelen, M., et al. (2022). Review of degradation and failure phenomena in photovoltaic modules. Renewable and Sustainable Energy Reviews *159*, 112160. 10.1016/J.RSER.2022.112160.

29. Macário, D., Domingos, I., Carvalho, N., Pinho, P., and Alves, H. (2022). Harvesting circuits for triboelectric nanogenerators for wearable applications. iScience *25*, 103977. 10.1016/J.ISCI.2022.103977.

30. Wang, J., Xu, S., Zhang, C., Yin, A., Sun, M., Yang, H., Hu, C., and Liu, H. (2023). Field effect transistor-based tactile sensors: From sensor configurations to advanced applications. InfoMat *5*, e12376. 10.1002/INF2.12376.

31. Zhang, C., Li, S., He, Y., Chen, C., Jiang, S., Yang, X., Wang, X., Pan, L., and Wan, Q. (2020). Oxide Synaptic Transistors Coupled with Triboelectric Nanogenerators for Bio-Inspired Tactile Sensing Application. IEEE Electron Device Letters *41*, 617–620. 10.1109/LED.2020.2972038.

32. Bu, T., Xu, L., Yang, Z., Yang, X., Liu, G., Cao, Y., Zhang, C., and Wang, Z.L. (2020). Nanoscale triboelectrification gated transistor. Nature Communications 2020 11:1 *11*, 1–8. 10.1038/s41467-020-14909-6.

33. Zhao, L., Chen, K., Yang, F., Zheng, M., Guo, J., Gu, G., Zhang, B., Qin, H., Cheng, G., and Du, Z. (2019). The novel transistor and photodetector of monolayer MoS2 based on surface-ionic-gate modulation powered by a triboelectric nanogenerator. Nano Energy *62*, 38–45. 10.1016/J.NANOEN.2019.05.012.

34. Liu, Y., Zhong, J., Li, E., Yang, H., Wang, X., Lai, D., Chen, H., and Guo, T. (2019). Self-powered artificial synapses actuated by triboelectric nanogenerator. Nano Energy *60*, 377–384. 10.1016/J.NANOEN.2019.03.079.

35. Yu, J., Gao, G., Huang, J., Yang, X., Han, J., Zhang, H., Chen, Y., Zhao, C., Sun, Q., and Wang, Z.L. (2021). Contact-electrification-activated artificial afferents at femtojoule energy. Nature Communications 2021 12:1 *12*, 1–10. 10.1038/s41467-021-21890-1.

36. Wei, Y., Liu, W., Yu, J., Li, Y., Wang, Y., Huo, Z., Cheng, L., Feng, Z., Sun, J., Sun, Q., et al. (2022). Triboelectric Potential Powered High-Performance Organic Transistor Array. ACS Nano *16*, 19199–19209. 10.1021/ACSNANO.2C08420/SUPPL_FILE/NN2C08420_SI_001.PDF.

37. Yu, J., Yang, X., Gao, G., Xiong, Y., Wang, Y., Han, J., Chen, Y., Zhang, H., Sun, Q., and Wang, Z.L. (2021). Bioinspired mechano-photonic artificial synapse based on graphene/MoS2 heterostructure. Sci Adv *7*, 9117–9134. 10.1126/SCIADV.ABD9117/SUPPL_FILE/ABD9117_SM.PDF.

38. Cheng, L., Yu, J., Wei, Y., Feng, Z., Li, Y., Wang, Y., Xu, N., Wang, Z.L., and Sun, Q. (2023). Triboelectric-potential configurable MoTe2 homojunction for photovoltaic device and logic circuits. Nano Energy *114*, 108632. 10.1016/J.NANOEN.2023.108632.

39. Kim, W.G., Kim, D.W., Tcho, I.W., Kim, J.K., Kim, M.S., and Choi, Y.K. (2021). Triboelectric Nanogenerator: Structure, Mechanism, and Applications. ACS Nano *15*, 258–287. 10.1021/ACSNANO.0C09803/ASSET/IMAGES/MEDIUM/NN0C09803_0020.GIF.

40. Shin, H., and Kim, D.Y. (2022). Rotating Gate-Driven Solution-Processed Triboelectric Transistors. Sensors 2022, Vol. 22, Page 3309 *22*, 3309. 10.3390/S22093309.

41. Kim, Y., Wu, X., and Oh, J.H. (2020). Fabrication of triboelectric nanogenerators based on electrospun polyimide nanofibers membrane. Scientific Reports 2020 10:1 *10*, 1–9. 10.1038/s41598-020-59546-7.

42. Hamilton, M.C., Martin, S., and Kanicki, J. (2004). Thin-film organic polymer phototransistors. IEEE Trans Electron Devices *51*, 877–885. 10.1109/TED.2004.829619.

43. Shin, E.C., Ko, J.H., Lyeo, H.K., and Kim, Y.H. (2022). Derivation of a governing rule in triboelectric charging and series from thermoelectricity. Phys Rev Res *4*, 023131. 10.1103/PHYSREVRESEARCH.4.023131/FIGURES/9/MEDIUM.

44. Brotherton, S.D. (2013). Introduction to thin film transistors: Physics and technology of TFTs. Introduction to Thin Film Transistors: Physics and Technology of TFTs *9783319000022*, 1–488. 10.1007/978-3-319-00002-2/COVER.

45. Pierret, R.F. (1983). Field effect devices. 116.

46. Dimaria, D.J. (1997). Explanation for the oxide thickness dependence of breakdown characteristics of metal-oxide-semiconductor structures. Microelectron Eng *36*, 317–320. 10.1016/S0167-9317(97)00072-5.

47. Li, W.Y., Ru, G.P., Jiang, Y.L., and Ruan, G. (2011). Trapezoid mesa trench metal-oxide semiconductor barrier Schottky rectifier: an improved Schottky rectifier with better reverse characteristics. Chinese Physics B *20*, 087304. 10.1088/1674-1056/20/8/087304.

48. Jin, H., Dong, S., Miao, M., Jei Liou, J., and Yang, C.Y. (2011). Breakdown voltage of ultrathin dielectric film subject to electrostatic discharge stress. J Appl Phys *110*. 10.1063/1.3633527/991768.

49. Griffiths, T.R., and Pugh, D.C. (1979). Correlations among solvent polarity scales, dielectric constant and dipole moment, and a means to reliable predictions of polarity scale values from cu. Coord Chem Rev *29*, 129–211. 10.1016/S0010-8545(00)82109-8.

50. Zou, H., Guo, L., Xue, H., Zhang, Y., Shen, X., Liu, X., Wang, P., He, X., Dai, G., Jiang, P., et al. (2020). Quantifying and understanding the triboelectric series of inorganic non-metallic materials. Nature Communications 2020 11:1 *11*, 1–7. 10.1038/s41467-020-15926-1.

51. Shin, H., Park, J., Baang, S., and Choi, J.S. (2020). Illumination Effect on Electrical Characteristics of Poly(3-hexylthiophene-2,5-diyl) Thin-Film Transistors. J Nanosci Nanotechnol *20*, 4368–4372. 10.1166/JNN.2020.17590.

52. Padurariu, L., Brunengo, E., Canu, G., Curecheriu, L.P., Conzatti, L., Buscaglia, M.T., Stagnaro, P., Mitoseriu, L., and Buscaglia, V. (2023). Role of Microstructures in the Dielectric Properties of PVDF-Based Nanocomposites Containing High-Permittivity Fillers for Energy Storage. ACS Appl Mater Interfaces *15*, 13535–13544. 10.1021/ACSAMI.2C23013/ASSET/IMAGES/LARGE/AM2C23013_0009.JPEG.

53. Arshad, A.N., Wahid, M.H.M., Rusop, M., Majid, W.H.A., Subban, R.H.Y., and Rozana, M.D. (2019). Dielectric and structural properties of poly(vinylidene fluoride) (PVDF) and poly(vinylidene fluoride-trifluoroethylene) (PVDF-TrFE) filled with magnesium oxide nanofillers. J Nanomater *2019*. 10.1155/2019/5961563.

54. Sharma, P.K., Gupta, N., and Dankov, P.I. (2020). Characterization of polydimethylsiloxane (PDMS) as a wearable antenna substrate using resonance and planar structure methods. AEU - International Journal of Electronics and Communications *127*, 153455. 10.1016/J.AEUE.2020.153455.

55.   Inagaki, N., Tasaka, S., and Park, Y.W. (2012). Effects of the surface modification by remote hydrogen plasma on adhesion in the electroless copper / tetrafluoroethylene - hexafluoropropylene copolymer (FEP) system. http://dx.doi.org/10.1163/156856198X00768 *12*, 1105–1119. 10.1163/156856198X00768.

56.   Tofel, P., Částková, K., Říha, D., Sobola, D., Papež, N., Kaštyl, J., Ţălu, Ş., and Hadaš, Z. (2022). Triboelectric Response of Electrospun Stratified PVDF and PA Structures. Nanomaterials (Basel) *12*. 10.3390/NANO12030349.

57.   Zhang, R., and Olin, H. (2020). Material choices for triboelectric nanogenerators: A critical review. EcoMat *2*. 10.1002/EOM2.12062.

Figure 1. Schematic overview of the fabricated AFRGT

The fabricated AFRGT featuring a cylindrical aluminum gate with a polyimide surface. The rotating gate is positioned at an air gap distance from the active layer and rotates along the path indicated by the red dotted arrow.

Figure 2. Schematic diagrams showing the mechanism of channel formation within the fabricated AFRGT

(a) Cross-sectional schematic of the device structure, (b) generation of triboelectric charges due to the presence of aluminum with covered polyimide surface, (c) configuration of the rotating gate and the main body of the AFRGT with an air-gap distance, (d) friction interactions with microscopic airborne particles within the air gap as the gate initiates rotation in the direction indicated by the orange arrow, (e) negatively charged particles influenced by polyimide, (f) induction of negatively charged particles resulting in the majority carriers in the active layer on the surface, and (g) an insulating substrate polarization facilitating hole-carrier accumulation.

Figure 3. Schematic diagram of drain current owing to holes

Schematic diagram depicting the flow and amplification of drain current when a drain voltage is applied to both ends of the channel established within the active layer of (a) an AFRGT and (b) a conventional FET when a gate voltage is applied. (c) Energy level diagram between the source and drain electrodes when the drain voltage is below zero for the P-channel transistors in both the AFRGT and conventional FET. Holes migrate along the path indicated by the red-dotted arrow.

Figure 4. Output characteristics of the AFRGT

The AFRGT with (a) a bare aluminum gate and (b) a polyimide-covered gate under both stopped and rotating conditions. Drain current variations over time are observed under various drain voltage regulations ($V_D = 0, -5, -10, -15,$ and -20 V). The regions shaded in yellow correspond to gate rotation (i.e., driving), whereas the unshaded regions represent gate stopped (non-driven).

Figure 5. Variation in drain current for different PVDF substrate thicknesses

Variation in drain current according to drain voltage in the AFRGT (10, 50, 100, 150, and 200 μm) employing (a) a bare aluminum gate and (b) a polyimide-covered gate. The black squares denote variations in drain current recorded

during gate immobility, whereas the red circles represent measurements recorded during gate rotation. The rightmost graph contains the statistics for different thicknesses.

Figure 6. Drain current variations in the AFRGT with a 50 µm substrate

Curves demonstrating the variations as (a) the applied drain voltage gradually reduces from 0 to −5 V and (b) the air-gap distance progressively increases from 0.5 to 100 mm.

Figure 7. Variations in the drain current of to the AFRGT with glass, FEP, PDMS, and PVDF substrates

Variations in the drain current in response to drain voltage applied to the AFRGT under both stopping and rotating conditions: (a) bare aluminum gate and (b) polyimide-covered gate. The rightmost graph contains the statistics for different thicknesses.

Figure 8. Variations in drain current of the ARGT with no active layer

(a) an uncovered bare aluminum gate and (b) a polyimide-covered gate.

Figure 9. Procedure for validating the feasibility of using the current amplified from a tire of an RC car.

(a) Photograph of the actual AFRGT device enclosed within the square dotted outline. (Insets: Dotted arrows and structural schematics for part identification, as well as photographs showcasing the flexibility of the fabricated device). (b) Image of the flexible AFRGT securely affixed to a rigid frame for electrode connections and attachment, and (c) this frame subsequently attached with an air gap to a tire of an RC car. (d) Graph depicting drain current over time, alongside (e) and (f) actual photographs captured when the RC car is in motion and at rest. The demonstration video is available in the Supplemental Information (see Video S1 and S2).

STAR METHODS

KEY RESOURCES TABLE

REAGENT or RESOURCE	SOURCE	IDENTIFIER
Chemicals, peptides, and recombinant proteins		

PDMS	Sewang Hitech Silicone	Sylgard 184
P3HT	Rieke Metals	Cat#4002-EE
PVDF	Sigma-Aldrich,	CAS: 24937-79-9
Ag paste	ELCOAT	P-100
DMF	Sigma-Aldrich	CAS: 68-12-2
Cloroform	Sigma-Aldrich	CAS: 67-66-3
Software and algorithms		
OriginPro 8.5	OriginLab Corporation	https://www.originlab.com/
Other		
Keithley 2636 SourceMeter	Tektronix Technologies	https://www.tek.com/
Slide glass	Marienfeld	https://www.marienfeld-superior.com/
FEP film	BOLA	https://www.bola.de/

RESOURCE AVAILABILITY

Lead contact

Further information and requests for resources and materials should be directed to and will be fulfilled by the lead contact, Dae Yu Kim (dyukim@inha.ac.kr).

Materials availability

This study did not generate new unique materials.

Data and code availability

• This paper analyzes existing, publicly available data. These accession numbers for the datasets are listed in the key resources table.

• This paper does not report original code.

• Any additional information required to reanalyze the data reported in this paper is available from the lead contact upon request.

METHOD DETAILS

Figure 1 depicts a top-contact transistor featuring an aluminum rotating gate covered with a polyimide film. The rotating gate is situated 1 mm away from the P3HT active layer in which the air gap serves as the insulating layer in the transistor structure.

Preparation of the Device Substrates

Among the various types of AFRGT substrates, PVDF was prepared as follows. Initially, PVDF in the powder form (Sigma-Aldrich, Mw ~534,000) was mixed with N,N-Dimethylformamide (DMF, Sigma-Aldrich) at a concentration of 5 wt% and then dissolved using a sonicator for 10 min. The resulting solution was then poured onto a slide glass and annealed at 100 °C for 30 min on a hot plate to produce a flat PVDF substrate. For the PDMS substrate, Sylgard 184A was mixed with a curing agent (Sylgard 184B) in a 10:1 wt. ratio and stirred at 250 rpm for 10 min at room temperature. The solution was then applied to a slide glass and annealed at 100 °C for 30 min to form a flat PDMS substrate. The slide glass (Marienfeld) and FEP film (BOLA) were ultrasonically cleaned with acetone, isopropyl alcohol, and deionized water, after which the substrates were used as the glass and FEP substrates, respectively.

Fabrication of the AFRGTs

A 5 wt% solution of P3HT (Rieke Metals) dissolved in chloroform was drop-cast onto the prepared substrates, followed by thermal curing at 90 °C for 30 min. Subsequently, silver paste was applied to both top edges of the P3HT layer to serve as the S/D electrodes, resulting in a square active layer with a channel width (W) and length (L) of 17 mm. A rotating gate consisting of a polyimide-covered aluminum wheel with a width of 17 mm and a smooth surface was affixed to a motor and positioned at a 1 mm distance from the active layer of the AFRGT. This setup effectively replaced the conventional application of the gate electrode and V_G.
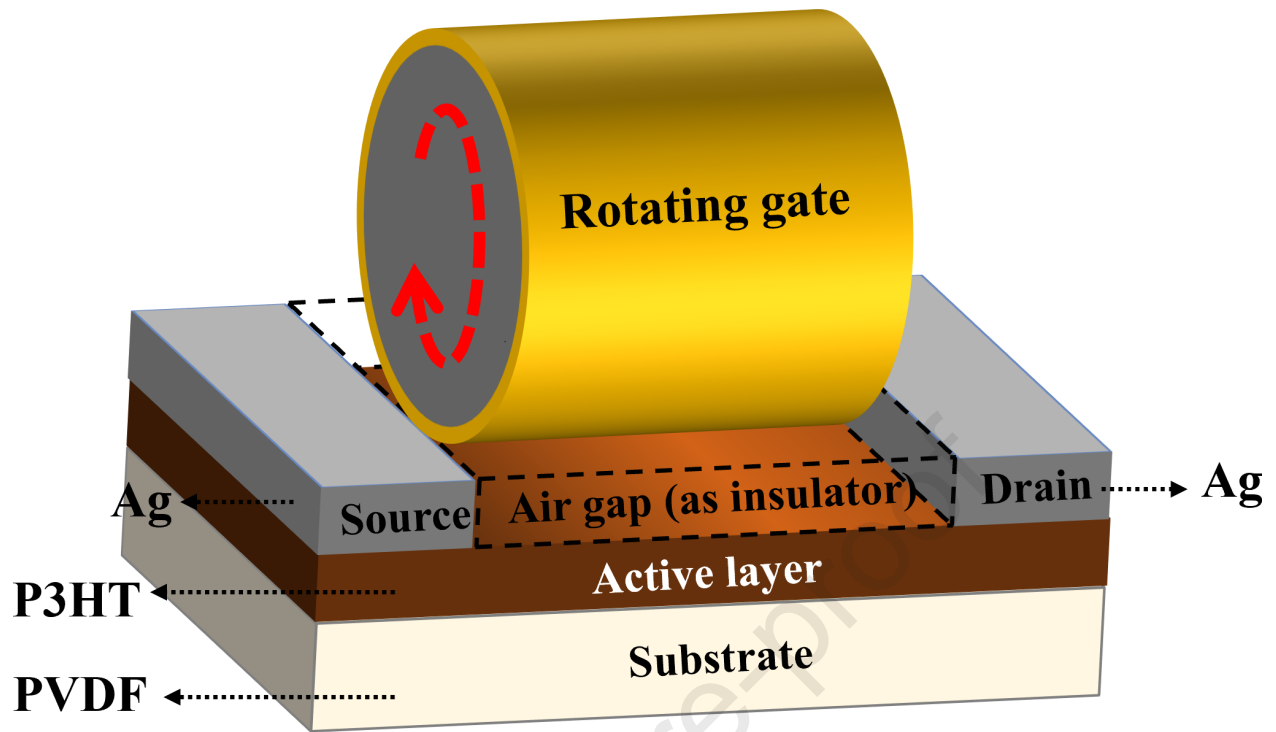
Measurement and Characterization

To assess the electrical characteristics of the fabricated AFRGT, we examined the I_D while the gate was rotated at a speed of 2200 rpm by a fixed motor, following the application of V_D between the S/D electrodes using the Keithley 2636 SourceMeter. To ensure that the observed drain current was generated by the rotating gate, we compared the drain current obtained under this rotational state to that obtained when the motor was stopped. This comparative analysis proved that the rotating gate was actively influencing the output current.
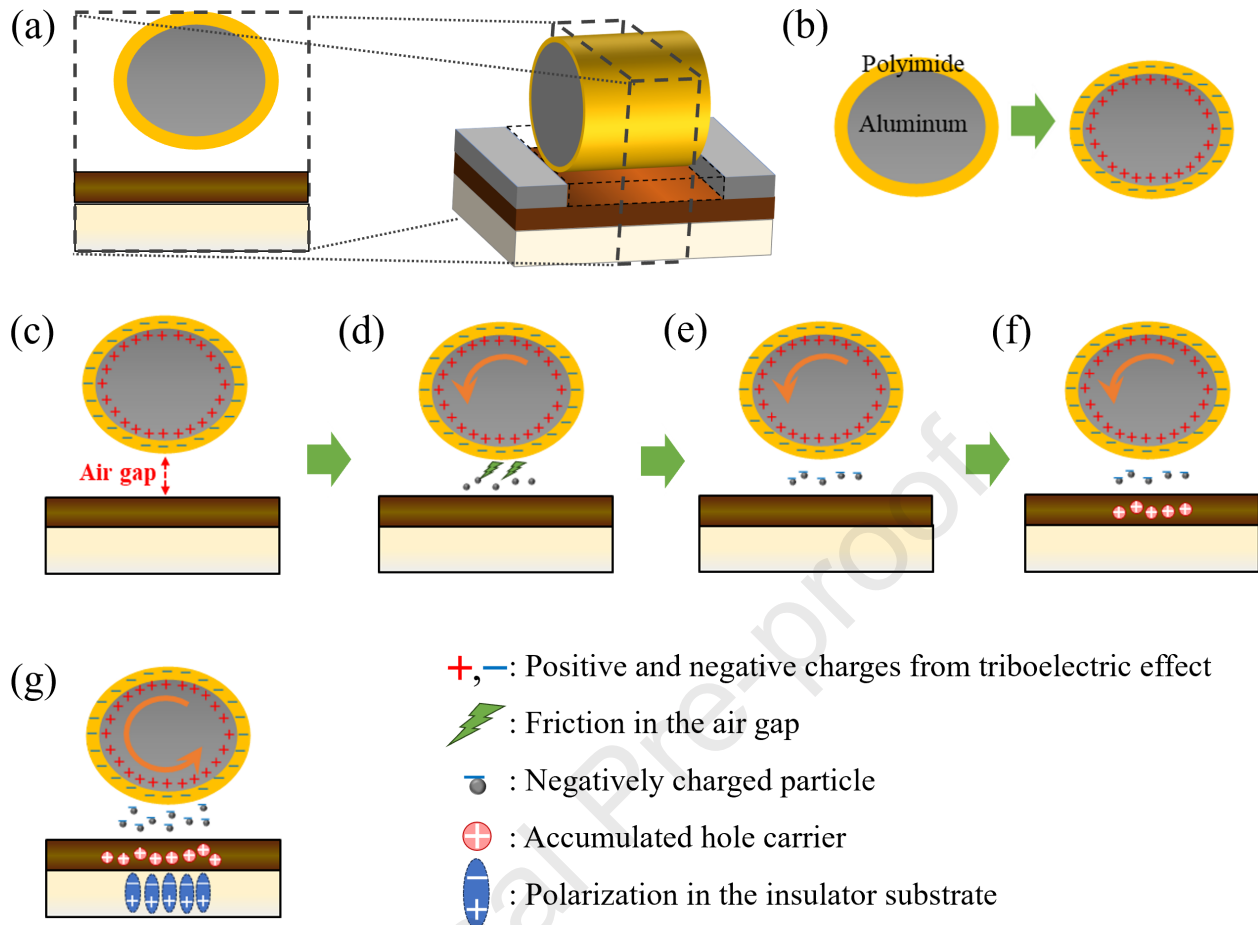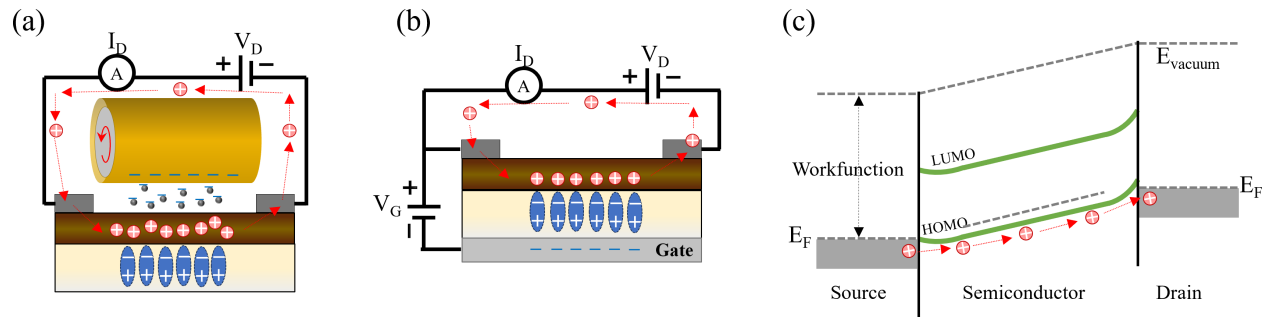
Supplemental Information

Video S1. The fluctuation of the drain current profile during forward, reverse, and stop motions of the RC car with a drain voltage of −20 V in Figure 9.

Video S2. The procedure for measuring drain current amplification during the swift rotation of RC car wheels under drain voltage conditions of −20 V or 0 V in Figure 9.
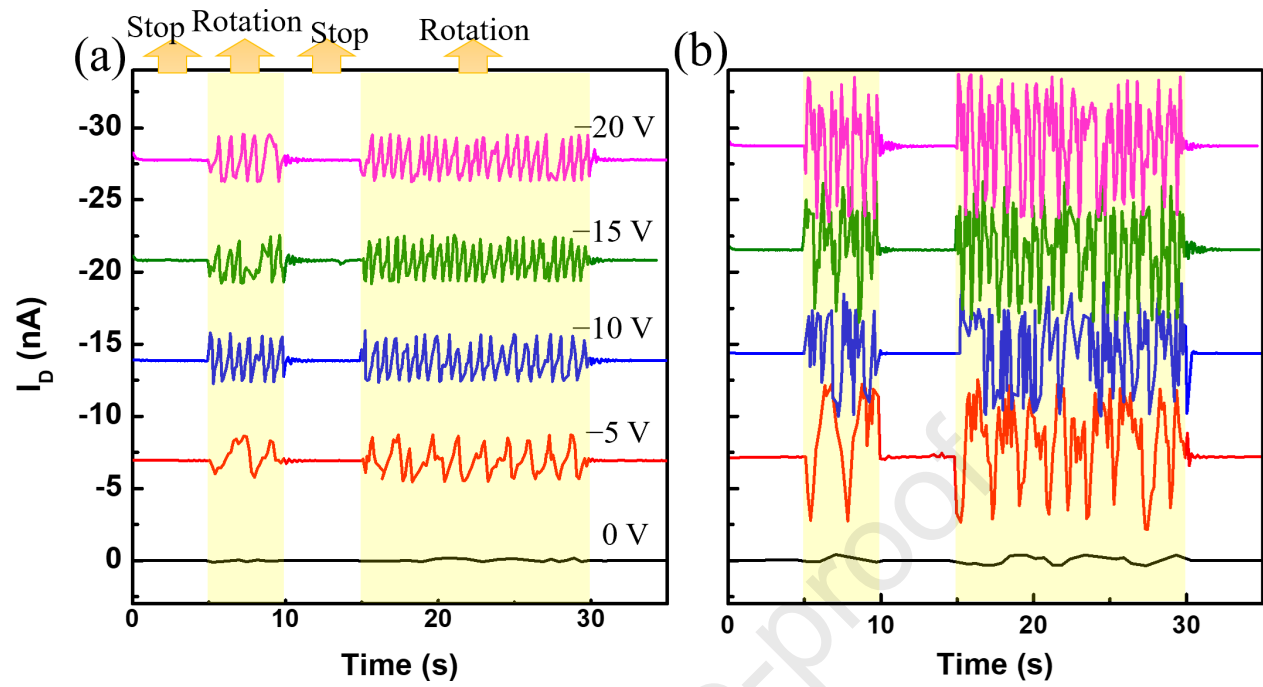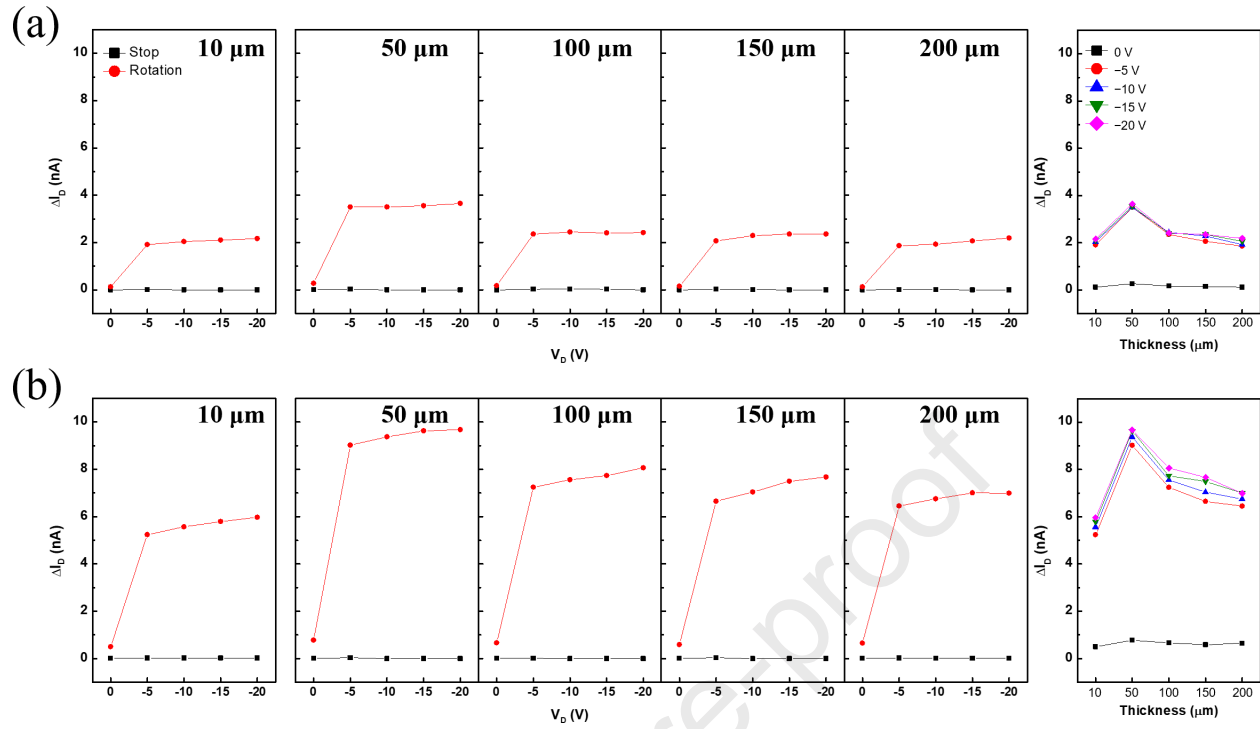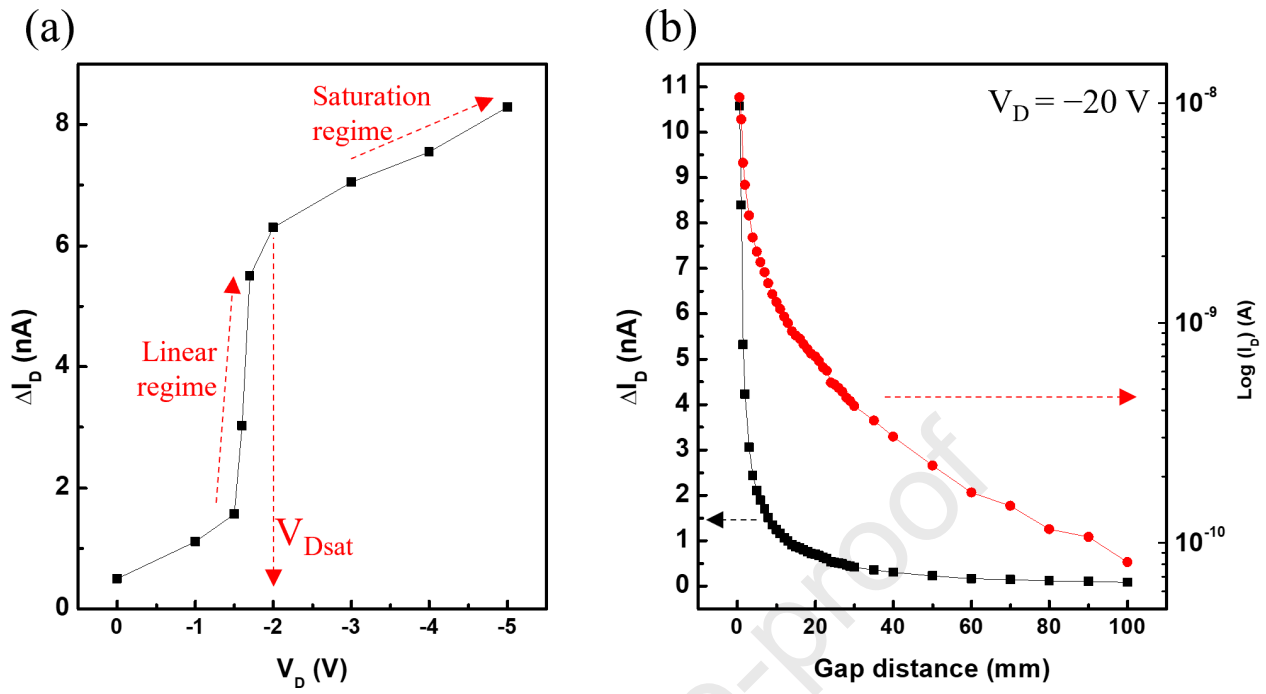
Rotating gate

Ag ←········· **Source** | **Air gap (as insulator)** | **Drain** ·······→ **Ag**

Active layer

P3HT ←·················

Substrate

PVDF ←·················

(a)

(b)

Polyimide

Aluminum

(c)

Air gap

(d)

(e)

(f)

(g)

$+$,$-$: Positive and negative charges from triboelectric effect

: Friction in the air gap

: Negatively charged particle

$\oplus$: Accumulated hole carrier
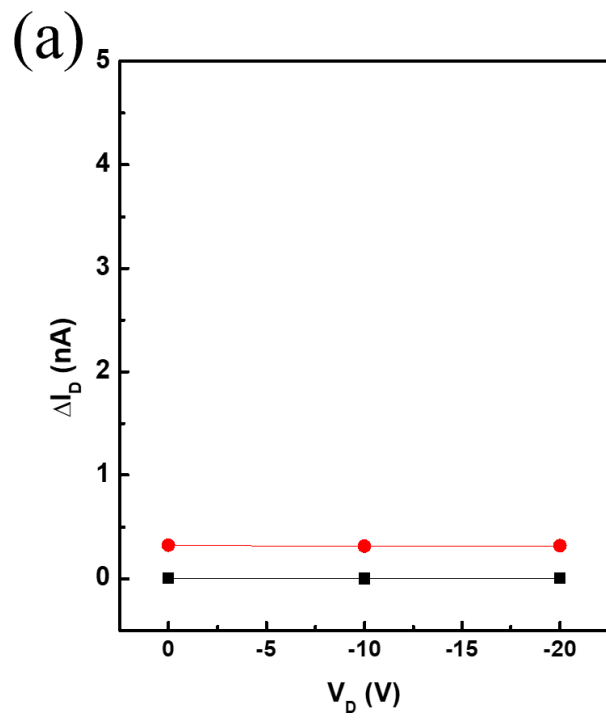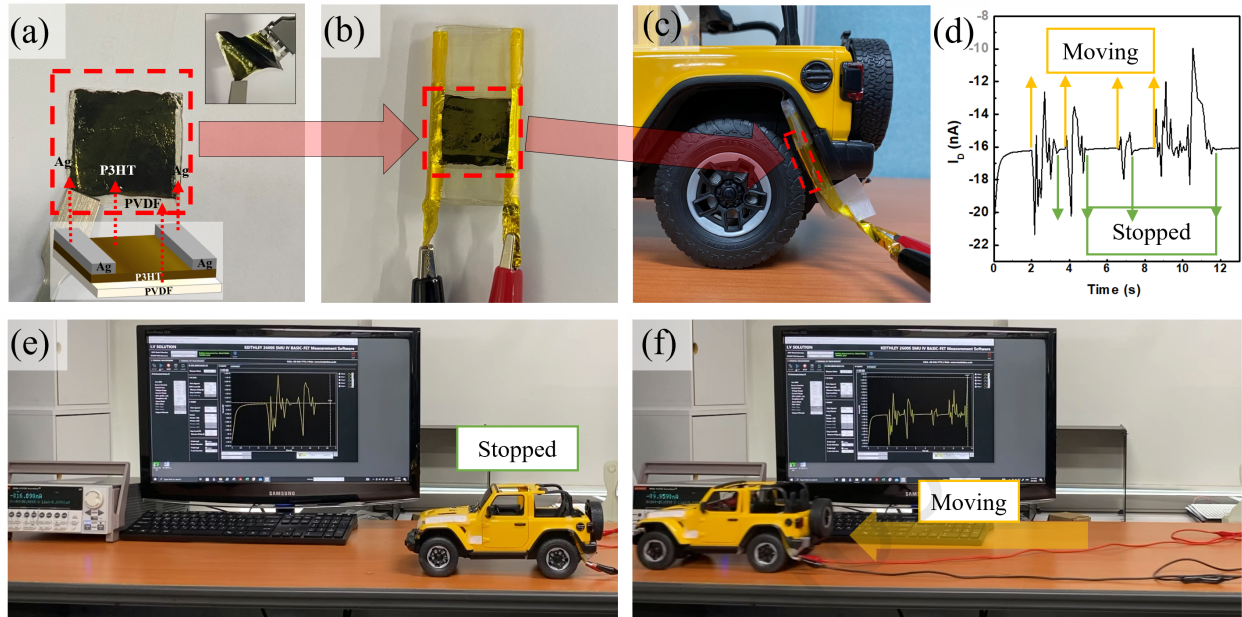
: Polarization in the insulator substrate

(a)

(b)
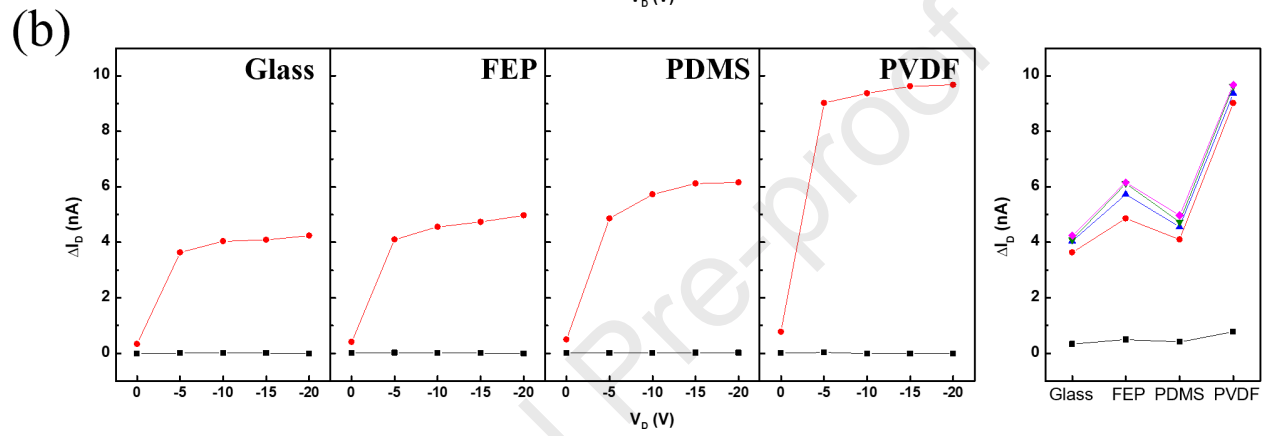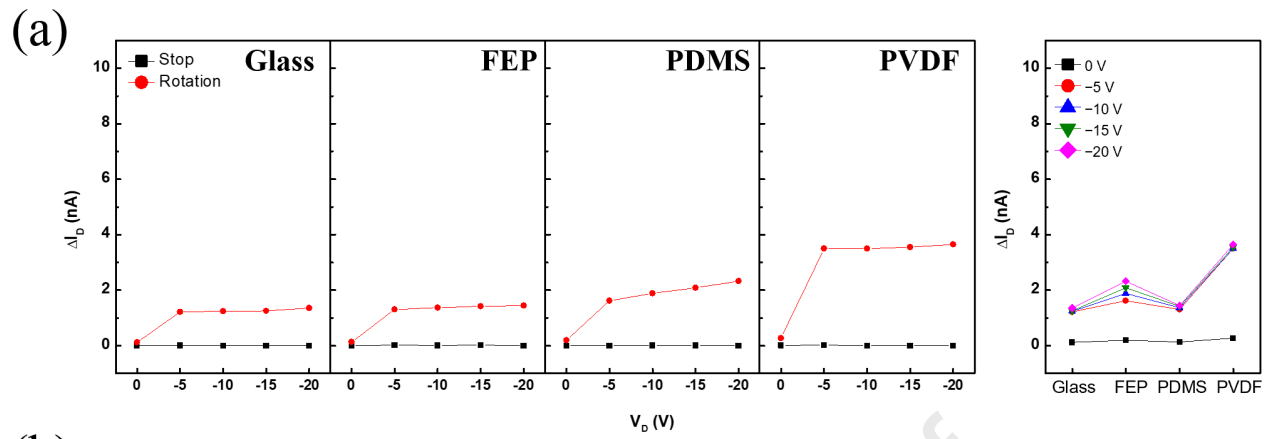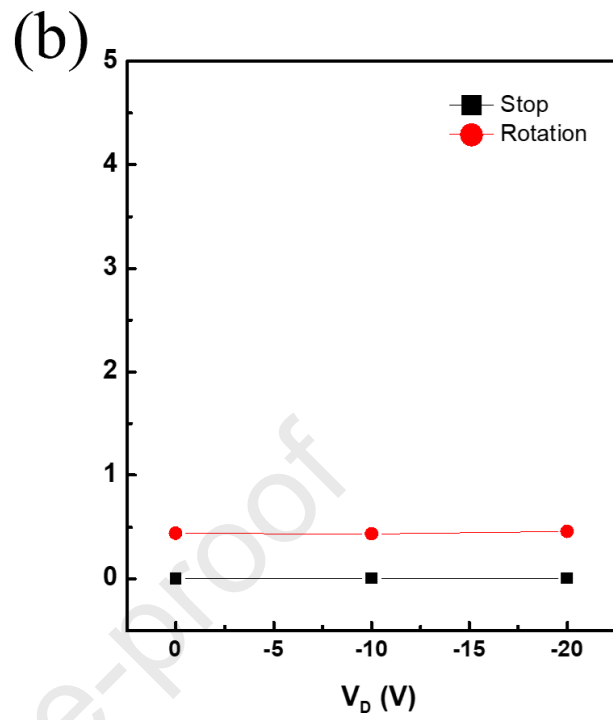
Highlights

·An innovative transistor operating without a gate voltage

·Wear-resistant, slim, and flexible with low-temperature processing

·Simplified three-layer structure reduces carbon emissions in manufacturing

·Harvests energy from vehicle tires, conveyor belts, or any moving part